Appl Phys B (2011) 104:175–188
DOI 10.1007/s00340-011-4448-9

Applied Physics B
Lasers and Optics

Spectrally resolved light absorption properties of cooled soot from a methane flame

A.R. Coderre · K.A. Thomson · D.R. Snelling · M.R. Johnson

Received: 13 September 2010 / Revised version: 13 December 2010 / Published online: 16 March 2011

Abstract The optical properties of combustion-generated soot, crucial information for quantitative soot emission diagnostics and for climate modeling, have been determined for the particular case of cooled soot from a methane flame. Optical extinction measurements were performed over a wavelength range of 450–750 nm using a novel diffuse-light, spectrally resolved line-of-sight attenuation experiment, and quantified using extractive methods coupled with scanning and transmission electron microscopy in conjunction with a detailed uncertainty analysis. The absorption component of the total measured extinction was isolated by calculating the expected scattering contribution, according to the Rayleigh–Debye–Gans approximation for polydisperse fractal aggregates. In contrast to the large degree of scatter seen in data previously reported in the literature, a consistent trend of negligible variation of the soot absorption refractive index function $E(m)$ with wavelength over the visible was observed ($E(m) = 0.35 \pm 0.03$ at wavelengths of 450–750 nm). These new data are also cast in the form of dimensionless extinction, which is independent of the scatter correction, as well as mass absorption cross section, which is independent of the mass density of soot and is commonly used by atmospheric modelers.

A.R. Coderre · M.R. Johnson (✉)
Mechanical and Aerospace Engineering, Carleton University, 1125 Colonel By Drive, Ottawa, Ontario K1S 5B6, Canada
e-mail: Matthew_Johnson@carleton.ca
Fax: +1-613-5205715

A.R. Coderre
e-mail: Adam.Coderre@gmail.com

K.A. Thomson · D.R. Snelling
Institute for Chemical Process and Environmental Technology, National Research Council of Canada, 1200 Montreal Road, Ottawa, Ontario K1A 0R6, Canada

K.A. Thomson
e-mail: Kevin.Thomson@nrc-cnrc.gc.ca
Fax: +1-613-9577869

D.R. Snelling
e-mail: Dave.Snelling@nrc-cnrc.gc.ca

1 Introduction

Combustion-generated soot is an atmospheric pollutant that has been shown to cause adverse health effects in humans and other animals [1] and contribute to climate change through radiative forcing [2, 3]. However, quantification of soot emissions has proven to be a challenging task. Optical diagnostics have been developed that promise to meet this challenge [4, 5], though their accuracy is limited by the level of accuracy to which the optical properties of soot are known [6–8], with Crosland et al. [8] showing a greater than 50% uncertainty in soot volume fraction measured by laser-induced incandescence (LII) due to uncertainty in the absolute value and spectral variation of the soot refractive index light absorption function, $E(m)$. Soot optical properties have been the focus of many studies using a variety of in-situ and ex-situ techniques for in-flame and over-fire soot (see [9] and references therein); however, there is a large variation in the reported optical properties and uncertainty regarding the equivalence of in-flame and over-fire soot optical properties [9–11]. Despite attempts to rationally eliminate some of the reported optical property data based on problems with the collection and/or analysis methods used [8, 9], uncertainty limits are still large for use in soot emission pyrometry based techniques [8]. Interestingly, despite the prevalence of natural gas as a fuel (accounting for more than a fifth of the world's total primary energy supply [12]), very few studies of soot properties [13–15] have considered soot generated from methane, the primary con-

Table 1 Selected studies of soot optical properties

Study	Fuel	λ [nm]	In/ex-situ	Method
Dalzell and Sarofim [26]	C_2H_2, C_3H_6	436–10000	Ex-situ	Reflectance
Lee and Tien [24]	Polymers	Visible	In-situ	Dispersion model
Mullins and Williams [13]	Various	450, 633	Ex-situ	Reflectance/extinction
Chang and Charalampopoulos [27]	C_3H_6/O_2	200–6400	In-situ	Scattering/extinction
Bruce et al. [28]	Diesel	Various	In-situ	Photoacoustic
Stagg and Charalampopoulos [25]	C_3H_6/O_2	400–700	Ex-situ	Ellipsometry
Dobbins et al. [29]	Crude oil	450–1000	In-situ	Extinction
Köylü and Faeth [30]	Various	200–5200	In-situ	Extinction
Krishnan et al. [31]	Various	351–800	In-situ	Scattering/extinction
Schnaiter et al. [32]	Diesel	450–700	In-situ	Scattering/extinction
Snelling et al. [33, 35]	C_2H_4	436–1064	In-situ	Pyrometry/LII

stituent of natural gas. These few studies do not consider post-flame, cooled soot such as would be found as emissions from various engine and industrial processes. The measurements are done with monochromatic light sources, such as lasers, providing data at only discrete points of the spectrum and do not provide uncertainty estimates of the determined optical properties. Therefore, the goals of the present work include filling in the missing property information for cooled, post-flame soot from methane fuel over a wide range of wavelengths, achieved through the use of an optical diagnostic capable of measuring extinction over a continuous range of wavelengths, and performing a detailed uncertainty analysis on the results.

1.1 Soot morphology

Soot consists of many small carbonaceous spherules of near-constant diameter, called primary particles, that aggregate together to form branching, chain-like structures. Such geometry cannot be approximated successfully using dense or porous spheres, or any other simple shapes [16]; however, it has been shown [17, 18] that soot aggregates are well described as mass-fractal-like, where the number of primary particles, N, that make up an aggregate can be related to the aggregate radius of gyration, R_g, and the primary particle diameter, d_p, by (1), where D_f is the fractal dimension and k_g is the fractal prefactor.[1]

$$N = k_g \left(\frac{R_g}{d_p} \right)^{D_f}. \tag{1}$$

[1] Some researchers [16, 19, 20] adopt an alternate definition using the primary particle radius, a, in place of the diameter, which results in different values for the fractal prefactor. One might argue that this definition is more consistent in that it contains a ratio of radii; however, the diameter is the measured quantity and it is desirable to use that value directly. To avoid confusion, we will adopt the term k_g as the prefactor defined using the diameter as in (1) and k_f as the prefactor when using the radius instead. The relationship between the two is $k_f = k_g (1/2)^{D_f}$.

A probability distribution function (PDF) is used to describe the probability that a randomly selected aggregate contains N primary particles. This distribution, when multiplied by the number concentration of aggregates, gives the aggregate size distribution per unit volume, which describes the number concentration of aggregates as a function of N. A self-preserving, scaling distribution describes aggregating systems well [19, 21, 22]. For $N > N_{avg}$ (most important from a light scattering perspective), van Dongen and Ernst [22] have derived a form of the self-preserving distribution, which is also summarized in Appendix B of [19]. Sorensen has shown [19, 23] that this distribution effectively describes scattering from fractal aggregates; therefore, it was selected for use in the present work.

1.2 Current knowledge of soot optical properties

The optical properties of soot have seen much attention in the past, and the methods used to obtain them are as widely varied as the results [13–15, 24–33]. It is often the case that values reported in the literature are used generically, despite the specific nature of the experiments used to obtain these data. Table 1 compares the approaches of several relevant previous studies, and their results will be compared to the present results in Fig. 3 below, which shows variability in the reported results by about a factor of three.

To date, most work on soot optical properties has focused on soot sampled or measured in-flame rather than from an exhaust pipe or smoke stack, which does not necessarily reflect the latter conditions. In fact, some groups [24] have predicted a significant change in optical properties with temperature, which conflicts with other studies that found none [25]. Further measurements at ambient conditions are therefore necessary.

As mentioned above, soot from methane flames is rarely if ever considered, perhaps due to methane's low sooting propensity; only a small number of measurements of methane soot properties, typically using now-outdated opti-

cal and soot characterization methods, were found in the literature [13–15]. (Therssen et al. [34] have also measured the relative difference in methane soot absorption at two wavelengths, but do not provide absolute measurements.)

2 Experimental approach

The accuracy of optical diagnostics is limited by the accurate knowledge of soot optical properties, in particular the absorption refractive index function, $E(m)_\lambda$ (hereafter referred to as simply the absorption function). This function is defined, along with its counterpart, the scattering refractive index function $F(m)_\lambda$, as follows, where $m = n - \mathrm{i}k$ is the complex index of refraction of soot and the subscript λ indicates the wavelength at which to evaluate the function:

$$E(m) = \Im\left(\frac{m_\lambda^2 - 1}{m_\lambda^2 + 2}\right), \tag{2}$$

$$F(m) = \left|\frac{m_\lambda^2 - 1}{m_\lambda^2 + 2}\right|^2. \tag{3}$$

Using the Rayleigh–Debye–Gans approximation for polydisperse fractal aggregates (RDG-PFA), which has been shown to provide good estimates (within 10% uncertainty) of optical cross sections for soot aggregates where light absorption typically dominates over total scatter [23, 36–40], the volumetric extinction coefficient, $K_{\mathrm{ext},\lambda}$, can be related to the soot volume fraction, f_v, through the following relation:

$$K_{\mathrm{ext},\lambda} = \frac{6\pi(1+\rho_{\mathrm{sa}})E(m)_\lambda}{\lambda} f_v, \tag{4}$$

where $\rho_{\mathrm{sa},\lambda} = K_{\mathrm{sca},\lambda}/K_{\mathrm{abs},\lambda}$ is the ratio of scattering-to-absorption coefficients. Equation (4) can be used as the governing equation for optical extinction measurements of soot, provided that the aggregates consist of primary particles that are within the Rayleigh limit ($\pi d_p/\lambda \ll 1$, generally taken to be $\pi d_p/\lambda < 0.3$, and $(\pi d_p/\lambda)|m| \ll 1$) [41]. Thus, finding $E(m)_\lambda$ required determination of three separate experimental quantities: the soot volume fraction f_v, the scattering-to-absorption ratio, $\rho_{\mathrm{sa},\lambda}$, and the spectral extinction coefficient $K_{\mathrm{ext},\lambda}$. Soot volume fractions were determined by gravimetric analysis. Determination of the scattering-to-absorption ratio first required knowledge of the soot morphology, which was found by a combination of scanning and transmission electron microscopy; this morphological information (d_p, N, D_f, k_g, and aggregate size distribution) was then used to support numerical calculation of $\rho_{\mathrm{sa},\lambda}$. Finally, $K_{\mathrm{ext},\lambda}$ was determined through diffuse-light spectral line-of-sight attenuation measurements. A detailed uncertainty analysis was performed to estimate and propagate the uncertainty in the results, as outlined in Appendix.

The soot under study was generated using an inverted co-flow diffusion-flame burner, capable of generating soot in a wide range of sizes and concentrations, based on the work of Stipe et al. [42]. A brief description of the burner follows, and the reader is referred to [43] for a more detailed description of the burner.

The inverted burner consists of three main sections: the burner head, the combustion chamber, and the exhaust tube. The layout of the burner and a cross-sectional view of the burner head can be seen in Fig. 1. The fuel tube (port 1) passes through the head and into the combustion chamber, and the co-flow combustion air enters a plenum through port (2) where the flow is distributed evenly by glass beads and passed through a layer of sintered metal foam into the combustion chamber. The combustion chamber consists of a vertical quartz tube through which the operator can visually monitor the flame. The burner exhaust tube consists of two parts: a stainless-steel pipe in which the flow mixes and cools, followed by a section of acrylonitrile–butadiene–styrene (ABS plastic) tubing that turns and exhausts the flow at port (6), where soot diagnostics are performed. The steel pipe features a port near each end; port (3) serves as an inlet for secondary dilution gas flow, and port (4) is an auxiliary sampling port. The ABS tube turns the exhaust stream through 180° and drains any condensed water (which only occurs during the transient warm-up period) through port (5). The drain outlet was kept below water level to prevent mixing of the exhaust gas and open air. Arnott et al. [44] have shown that relative humidity values below 65% do not affect aerosol optics. For all present test conditions, the relative humidity values calculated from inlet flows and measured exhaust gas temperatures ranged from 20 to 50%.

The inverted flame burner was operated at 12 different flow settings to generate soot under various conditions, with three main variables of interest: dilution ratio, dilution temperature, and dilution gas. These flow settings are summarized in Table 2. Global equivalence ratios were determined assuming complete (ideal) combustion of CH_4 with air (consisting of 21% oxygen), according to $\phi = 2Q_{\mathrm{fuel}}/0.21Q_{\mathrm{air}}$, and dilution ratio (DR) was defined as the volumetric ratio of dilution gas to combustion products, which for methane fuel can be expressed as $\mathrm{DR} = Q_{\mathrm{dil}}/(Q_{\mathrm{fuel}} + Q_{\mathrm{air}})$.

2.1 Gravimetric analysis

Gravimetric analysis is an ex-situ technique in which all particles from a known gas volume, V, are collected and weighed to determine the mass of soot collected, m_s. This is typically achieved through filter sampling of the aerosol while monitoring the gas velocity and sampling duration. If the particle density, ρ_s, is known, and the total gas volume drawn through the filter is measured, a non-dimensional volume fraction, f_v, can be obtained that is independent of the

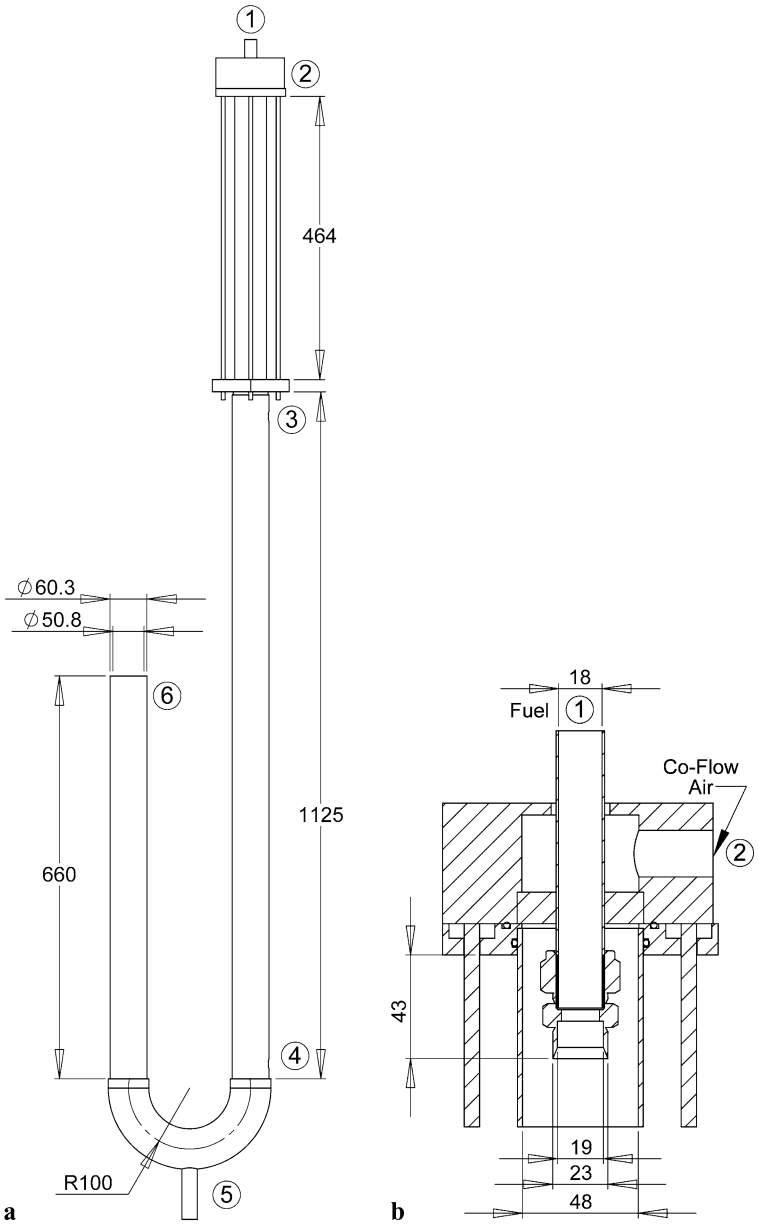

Fig. 1 (**a**) Layout of the burner system and (**b**) cross section of the burner head. Dimensions are in millimeters

optical properties of the particles:

$$f_v = \frac{m_s}{\rho_s V}\frac{T_s}{T_\infty}, \tag{5}$$

where the volume measurement is corrected for differences in temperature between the exhaust plume, T_s, and at the point of measurement (ambient), T_∞. The gravimetric soot volume fraction can be used to 'calibrate' optical diagnostics by inverting the governing equation (i.e. (4)) to solve for the missing property information rather than the soot volume fraction. This method has been used in the past [31, 45]. Note that the low sooting propensity of methane was compensated for by using a longer sampling time, such that the collected mass of soot, and thereby the accuracy of the measurement, was unaffected.

Soot was sampled from the exhaust plume using an isokinetic sampling system, which matches the velocity of the gas being sampled with that of the surrounding exhaust stream. The exhaust velocity profile was measured by a pitot tube traversed at the outlet, and average velocity found by continuity from the total input flow rate, corrected for temperature. Membrane filters (Whatman, Anodisc 25-mm diameter) with a pore size of 0.02 μm were used for soot collection, and weight measurements were made with an electronic micro-balance (Mettler Toledo, UMX2) both before and after soot was collected. The volume of exhaust gas from which the soot was collected was measured using a thermal mass flow meter (Brooks, SMART series), which was positioned downstream of the filter to avoid contamination by soot deposition. The exhaust gas temperature was

Table 2 Summary of burner settings

Label	Q_{fuel} [SLPM]	Q_{air} [SLPM]	Q_{dil} [SLPM]	Diluent (air/N_2)	T_{dil} [°C]	ϕ (global)	DR (vol.)
A1	1.2	15	50	N_2	25	0.76	3.1
B1	1.4	13	50	Air	25	1.03	3.5
B2	1.4	13	50	N_2	25	1.03	3.5
C1	1.2	15	50	Air	100	0.76	3.1
C2	1.2	15	50	Air	60	0.76	3.1
C3	1.2	15	50	Air	25	0.76	3.1
D1	1.2	15	40	Air	100	0.76	2.5
D2	1.2	15	40	Air	60	0.76	2.5
D3	1.2	15	40	Air	25	0.76	2.5
E1	1.2	15	30	Air	100	0.76	1.9
E2	1.2	15	30	Air	60	0.76	1.9
E3	1.2	15	30	Air	25	0.76	1.9

monitored with a thermocouple and had an average value of 56°C. These data were acquired at a rate of 10 Hz (hardware-timed). In addition to the uncertainties related to these measurements, there are several sources of uncertainty in the procedure, including vibration of the balance, electrostatic charges, the mass of contaminants retained in the filter along with the soot (e.g. moisture), and buoyancy effects due to fluctuations in the temperature and humidity of the filter conditioning environment [46]. Balance vibration was addressed by isolating the balance with an air suspension isolation table (Kinetic Systems Inc., Vibraplane). Buoyancy and moisture effects were reduced by conditioning the samples in a climate-controlled clean room (25°C and 50% relative humidity) for a minimum of 24 h prior to weighing [46, 47], and electrostatic charges on the samples were neutralized with an alpha-radiation neutralizer (Staticmaster, 2U500).

A nominal value of 40 samples, chosen to provide a statistically significant number of measurements for the sake of reduced precision uncertainty, were made for each of the 12 conditions, although a small number were discarded due to flaws, breakage, or contamination. Included in this number were four control filters per condition, which were handled in the same way as the samples, only without collecting any soot. The controls were used to detect any drifting of the balance, and for each condition the recorded masses were adjusted by the mean deviation of the controls, which were typically less than one percent of the measured mass of soot. For each condition, 10 of the 40 samples were taken for each of four durations, 60, 80, 100, and 120 s, to ensure linearity of the measured soot volume fraction with sample time. Repeatability tests were performed to measure the sample-by-sample variability in the balance measurements, which was found to be significantly greater than the quoted precision of the balance. The soot density used in the calculation was 1.89 ± 0.07 g/cm^3, which represents the mean of several values found in the literature [29, 45, 48, 49], and the uncertainty (95% confidence) was assumed to be dominated by the precision uncertainty and found by treating these literature values as repeated measurements.

2.2 Soot characterization

The extinction measurements needed to be corrected for light scattering, which is strongly dependent on the size of the particles. Thus, it was important to have an accurate estimate of the soot morphology (primary particle size, fractal properties, size distribution) to determine the scattering correction.

The physical structure of soot can be found by extractive sampling and observation via electron microscopy. Studies have found that three-dimensional properties of aggregates can be inferred from two-dimensional projected images [50], and were reviewed by Brasil et al. [20], who outlined a 'recipe' for aggregate characterization. This recipe allows the recovery of key morphological parameters, such as N, D_f, and k_g, from the two-dimensional images.

Transmission electron microscopy (TEM) is the current standard method used to determine soot morphology [50, 51]. The key mechanism for this method of soot collection is thermophoresis (also known as thermodiffusion or the Soret effect), whereby particles migrate from a hot region to a cold one [52]. It has been previously shown [53] that thermophoretic sampling collects a representative sample, meaning that it is not biased with respect to particle size, making it the method of choice for sampling soot from hot gases. However, in the current case of a cooled exhaust stream (outlet temperatures of 50–60°C), the thermal gradient between the exhaust gases and the TEM grid at ambient temperature was small, resulting in a weak thermophoretic force. This called into question the unbiased nature of this method, and ultimately led to the conclusion

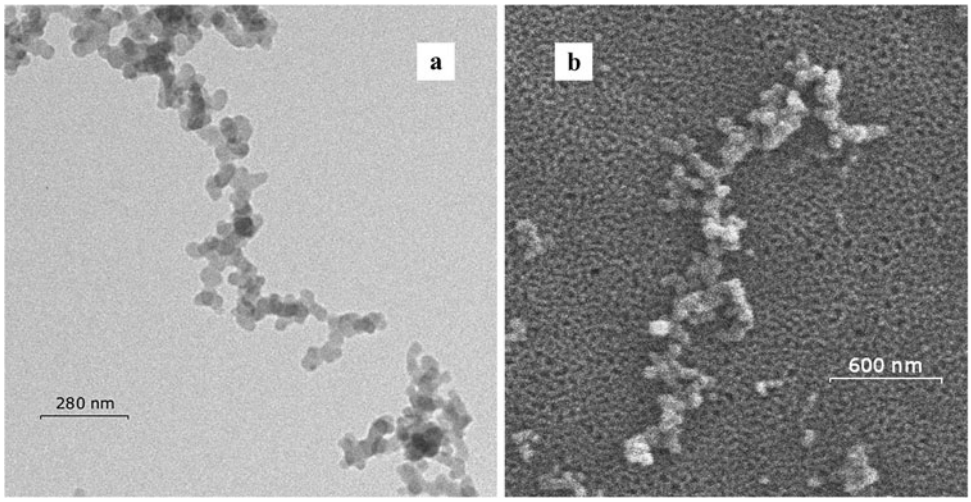

Fig. 2 Typical soot aggregates seen in (**a**) TEM and (**b**) SEM images

that thermophoretic sampling for TEM analysis (TS-TEM) was not appropriate for finding the aggregate size distribution in this case; scanning electron microscopy (SEM) was used instead, as is discussed below. However, since the primary particle size has been shown to be approximately uniform across a given soot sample [50], meaning that it is not a function of aggregate size and therefore unaffected by collection bias, TEM imaging was used to obtain d_p.

TEM sampling was performed using 3-mm carbon-coated copper grids (Electron Microscopy Sciences, cat. no. 71150), manually held in the exhaust stream for approximately one minute. Samples were imaged with a TEM (Philips, CM20) at a magnification of 18000×, and 80–100 measurements of d_p were made for each sampling condition, using Image Pro Plus 4.5.1 (Media Cybernetics). An example of a typical TEM image used for measurement is given in Fig. 2a.

To obtain the aggregate size distribution, filter sampling and subsequent analysis by SEM was performed. However, the nature of SEM requires the sample to be electrically conductive; for non-conductive samples such as soot, a thin coating of conductive material must be applied. This introduces some additional uncertainty in the projected area measurements taken from these images, but, for a soot aggregate several hundreds of nanometers in diameter, the uncertainty introduced by the conductive layer is small.

The SEM sampling apparatus was identical to that for the gravimetric analysis, only the sampling time was reduced to yield an appropriate surface coverage. The samples were coated with gold by sputter deposition with a thickness of 10 nm prior to imaging via SEM (JEOL, 840A). A typical SEM aggregate can be seen in Fig. 2b. The SEM microphotographs were analyzed according to the recipe given by Brasil et al. [20], also using Image-Pro Plus. The analysis of SEM images was considerably more difficult than for the standard TEM images, due primarily to the added complexity of separating aggregates from the background features (filter pores). Please refer to [43] for a detailed description of the image processing and aggregate characterization procedures. Aggregate size distributions were then found by fitting normalized histograms of the recovered N values to the self-preserving distribution, with the first moment M_1 and width parameter τ as the fitting parameters. The resulting mean primary particle size was $\bar{d}_p = 40.8$ nm, mean distribution parameters were $\bar{M}_1 = 79.8$ and $\bar{\tau} = 0.0$, and mean fractal parameters were $\bar{D}_f = 1.67$ and $\bar{k}_g = 7.87$.

2.3 Scattering-to-absorption ratio

The term $\rho_{\mathrm{sa},\lambda}$ is a ratio of the scattering-to-absorption coefficients; it is a function of the soot morphology (aggregate size distribution, fractal parameters, and primary particle diameter), the wavelength of light in question, and the ratio of scattering to absorption functions, $F(m)_\lambda / E(m)_\lambda$. The latter value is the only remaining unknown. Krishnan et al. [31] report an $F(m)_\lambda / E(m)_\lambda$ correlation for the wavelength range of 351–633 nm, which they found through their combined scattering/extinction measurements, gravimetric analysis, TEM, and reported values of k_g from the previous work of Köylü et al. [50]. They validated their findings by correcting the previous extinction measurements of Köylü and Faeth [30] with their current $\rho_{\mathrm{sa},\lambda}$ values to find $E(m)$, and then applying their $F(m)_\lambda / E(m)_\lambda$ correlation to determine $F(m)$. They found that their experimentally determined $E(m)$ and $F(m)$ and those extended from the work of Köylü and Faeth [30] agreed quite well for wavelengths above 400 nm. The correlation of Krishnan et al. [31] was curve fitted to a power-law relationship in order to extrapolate to the higher wavelengths considered here. The use of this curve-fit extrapolation likely introduces further uncertainty in this calculation; however, no other reasonable alternative was found. Of those studies listed above with

sufficient data to determine a correlation, most have been questioned in the past for one reason or another [30, 31]. For example, the ex-situ measurements made by Dalzell and Sarofim [26] and Stagg and Charalampopoulos [25] were performed on compressed soot pellets, which have been criticized for potentially altering the physical properties of soot. In addition, the earlier in-situ methods [24, 27] typically neglected characterization of soot morphology [30] and employed Rayleigh or Mie scattering theories, which have been found to be inappropriate for soot. Thus, the extrapolated correlation of Krishnan et al. [31] was deemed the most appropriate choice for this work. This choice is further justified by pointing out that the ratio $F(m)_\lambda/E(m)_\lambda$ serves only as a scaling factor in the $\rho_{\mathrm{sa},\lambda}$ calculation, which is itself a scaling factor applied to the measured extinction. As an example, with a typical calculated magnitude of $\rho_{\mathrm{sa},\lambda}$ of 20%, a 10% uncertainty in the ratio of $F(m)_\lambda/E(m)_\lambda$ only results in a 2% uncertainty in the scattering correction.

The ratio of scattering to absorption was calculated numerically from Rayleigh–Debye–Gans (RDG) theory using the approach of Sorensen [19]. Assuming that the soot primary particles are in the Rayleigh limit, and using RDG theory, the differential scattering cross section of an aggregate (i.e. the scattering cross section per unit solid angle) is given by [19]

$$\frac{d\sigma_{\mathrm{sca}}^{\mathrm{agg}}}{d\Omega} = k^4 F(m)\left(\frac{d_p}{2}\right)^6 N^2 S(q) = \frac{d\sigma_{\mathrm{sca}}^{\mathrm{pp}}}{d\Omega} N^2 S(q), \tag{6}$$

where $\frac{d\sigma_{\mathrm{sca}}^{\mathrm{pp}}}{d\Omega}$ is the differential scattering cross section of a single primary particle and $k = \frac{2\pi}{\lambda}$. The scattering vector $q(\theta)$ is given by $q(\theta) = [4\pi \sin(\theta/2)]/\lambda$.

The scattering cross section, which is a function of aggregate size N and scattering angle θ, can first be integrated over aggregate size N using the self-preserving distribution $P_{\mathrm{SP}}(N)$ with the defining parameters $\overline{M_1}$ and τ derived from SEM data,

$$\frac{d\sigma_{\mathrm{sca}}}{d\Omega} = \int_{N=1}^{N=\infty} P_{\mathrm{SP}}(N) \frac{d\sigma_{\mathrm{sca}}^{\mathrm{pp}}}{d\Omega} N^2 S(q)\, dN \tag{7}$$

and then, assuming RDG theory, integrating over 4π solid angle to give the total scattered light

$$\sigma_{\mathrm{sca}} = \int_{\phi=0}^{\phi=2\pi} \int_{\theta=0}^{\theta=\pi} \frac{d\sigma_{\mathrm{sca}}}{d\Omega}\left(1 + \left(\cos(\theta)\right)^2\right) \sin(\theta)\, d\theta\, d\phi. \tag{8}$$

The absorption cross section of an aggregate of size N is given by

$$\sigma_{\mathrm{abs}}^{\mathrm{agg}} = N \frac{\pi^2 d_p^3 E(m)}{\lambda}, \tag{9}$$

and integrating the absorption cross section over the distribution gives

$$\sigma_{\mathrm{abs}} = \overline{M_1} \frac{\pi^2 d_p^3 E(m)}{\lambda}. \tag{10}$$

The structure factor $S(q)$ was calculated using the complex hypergeometric approach of Sorensen [19]. The ratio of scattering to absorption, $\rho_{\mathrm{sa},\lambda}$, can now be calculated as the ratio of (8) to (10) using the assumed ratio of $E(m)_\lambda$ to $F(m)_\lambda$.

Uncertainty in $\rho_{\mathrm{sa},\lambda}$ was propagated parametrically, by repeating the calculation using the lower and upper 95% confidence limits of all the input parameters to observe the effect on the results. In addition, a blanket value of 10% uncertainty was added to account for inaccuracies of the RDG-PFA approximation, particularly at larger scattering angles [39, 40, 54]. The resulting combined uncertainties (95% confidence intervals) of $\rho_{\mathrm{sa},\lambda}$ were on the order of 20–30%, which, when acting alone, contributed actual uncertainties of only 3–5% to the calculated $E(m)_\lambda$ values since $E(m)_\lambda \propto 1/(1 + \rho_{\mathrm{sa},\lambda})$. For example, for a $\rho_{\mathrm{sa},\lambda}$ value of 0.2 with an uncertainty of 25%, as seen at a wavelength of 700 nm in Table 3 below, the effect on $E(m)_\lambda$ is $(1 + 0.2)/(1 + (0.2 \pm 0.05))$, or about 4%.

2.4 Spectral line-of-sight attenuation

Line-of-sight attenuation (LOSA) is a robust and direct optical method for the determination of the volumetric extinction coefficient, K_{ext}. K_{ext} can then be related to the soot volume fraction by (4), where the resulting soot volume fraction is proportional to $1/E(m)_\lambda$. The transmissivity, τ_λ, is defined as the ratio of the intensities of transmitted light (I_λ) to incident light ($I_{\lambda 0}$), and relates to the extinction coefficient $K_{\mathrm{ext},\lambda}$ using the Beer–Lambert Law [41, 55]:

$$\tau_\lambda = \frac{I_\lambda}{I_{\lambda 0}} = \exp\left(-\int_{-\infty}^{\infty} K_{\mathrm{ext},\lambda}(s)\, ds\right), \tag{11}$$

where s is the position along the optical path length through the medium, L. For the special case of an axisymmetric property medium, it is possible to invert the data using tomographic reconstruction to obtain a spatially resolved representation of the medium [55–57].

Advances in extinction measurements using long measurement cells, multi-pass cells, or cavity ring-down allow long measurement path lengths and thus very low detection limits suitable to ambient particulate concentration measurement (see [4] and references therein). However, the need for a measurement cell introduces potential sample bias problems such as particle–particle agglomeration and attrition to the cell walls. Furthermore, the measurement of concentrations typical of the exhaust of a smoking flame may push the upper limit of the dynamic range of these highly sensitive diagnostics.

For open-air measurement of potentially non-uniform aerosols such as flames or flame emissions, Greenberg and Ku [58] developed a two-dimensional LOSA (2D-LOSA) diagnostic based on expanded light sources, imaging optics, and charge-coupled devices. Snelling et al. [56] improved the method by replacing the laser with a collimated broadband light source, allowing a broader range of wavelengths to be tested. More recently, Thomson et al. [55] refined the method of Snelling et al. based on the use of a diffuse light source rather than a collimated one, allowing rejection of optical noise from the inevitable small aberrations present in the lenses, as well as addressing the problem of beam steering, resulting in a significantly improved sensitivity.

For the present requirement to measure the concentration field immediately downstream of the burner exit, and where significant gradients are only likely in the radial direction, a one-dimensional measurement was sufficient and thus the second dimension of the detector was available to measure attenuations in the spectral dimension. To achieve this, the diffuse LOSA method of Thomson et al. [55] was further modified to incorporate an imaging spectrometer (American Holographic, cat. no. SP00298-00) with the CCD (Princeton Instruments, 7386-0001). This allowed the acquisition of spectrally resolved extinction coefficients over the range of visible and near-infrared wavelengths of 450–950 nm. However, due to second-order effects in the spectrometer, data above 750 nm were found to be influenced by contributions from lower wavelengths and thus results for 450 to 750 nm only are reported. A halogen bulb was used instead of an arc lamp to improve the performance of the system over the wide spectral range. The lamp emission was fed into an integrating sphere, which produced uniform, diffuse light at its outlet. The halogen bulb was powered by a benchtop power supply to ensure a temporally constant emission. The use of diffuse light to make low-noise transmissivity measurements is discussed in detail in [55]. Thirty measurements were made for each condition, again using a statistically significant number to reduce the precision uncertainty. Three images were collected for each measurement, which were referred to as *plume*, *lamp*, and *dark*. The dark image was taken with the light source off and the plume blocked to account for ambient light and dark counts on the CCD. The lamp image was taken with the lamp on and the plume blocked, to measure the incident light. Finally, the plume image was taken with the lamp on and the plume flowing, to measure the transmitted light. The transmissivity of the plume, and thereby the extinction coefficient, was then found according to the relation

$$\tau_\lambda = \frac{\text{plume} - \text{dark}}{\text{lamp} - \text{dark}} = \frac{I_\lambda}{I_{\lambda 0}} = \exp\left(- \int_{-\infty}^{\infty} K_{\text{ext},\lambda}(s)\, ds \right). \tag{12}$$

A three-point Abel inversion method was employed to deconvolve the projected transmissivity data into a radial profile [59]. The inversion confirmed the uniformity of the soot concentration in the central region of the exhaust plume, where extinction measurements were performed. $K_{\text{ext},\lambda}$ values were determined using only the central region with radii from 0 to 5 mm. An annular integration was performed numerically over data within this range to obtain the averaged, spectrally resolved extinction coefficient. Note that while the inversion process enhances measurement noise, this noise is also averaged out through the annular integration. In this study, extinction coefficients ranged from 1.5 to 0.8 [1/m] while the diagnostic has a precision, principally limited by the short measurement length, of better than 0.035 [1/m] over most of the spectral measurement range. A detailed description of the analysis procedure can be found in [43] and the uncertainty of the measurements is included in the overall measurement uncertainty analysis detailed in Appendix.

3 Results and discussion

Data from the preceding diagnostics were combined according to (4) to quantify the wavelength-dependent soot absorption function $E(m)_\lambda$, as seen in Fig. 3. Although the differences in magnitude observable among the tested conditions were generally within calculated uncertainty limits (typically $\approx \pm 7\%$), these data were plotted against several relevant parameters specific to the experiment in an attempt to better understand the variability. These parameters included the measured physical or structural quantities of the soot ($D_f, k_g, d_p, N, R_g, f_v$), indirect quantities relating to soot formation calculated from experiment operating parameters (exhaust stream residence time, characteristic aggregation time), other experimental parameters (wavelength, dilution ratio), as well as several combinations of the above. However, no significant correlations were found.

The lack of correlation is perhaps unsurprising considering the relatively small variation in the $E(m)_\lambda$ results among conditions at a given wavelength; all measurements of $E(m)_\lambda$ fell within 20% of the mean, while the standard deviation among conditions was only 8–9% at all wavelengths. The $E(m)_\lambda$ values calculated for condition C3 were a slight outlier, without which the data fell within 10–13% of the mean and standard deviations dropped to 5–7%. The consistency in the $E(m)_\lambda$ data persisted despite large variations in several of the input parameters, including a near factor of two variation in the dilution ratio, which, coupled with the dilution air temperature variation, resulted in a 50% difference in the exhaust residence time.

The lack of variability in $E(m)_\lambda$ among the tested conditions suggests that, within uncertainty limits, the parame-

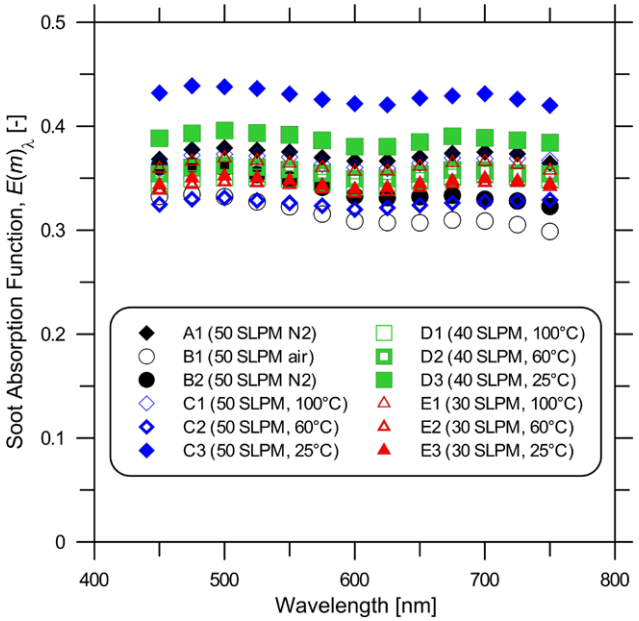

Fig. 3 $E(m)_\lambda$ results for each tested burner flow condition. For clarity, calculated uncertainties are not shown in the plot but were typically $\approx \pm 7\%$ for all conditions

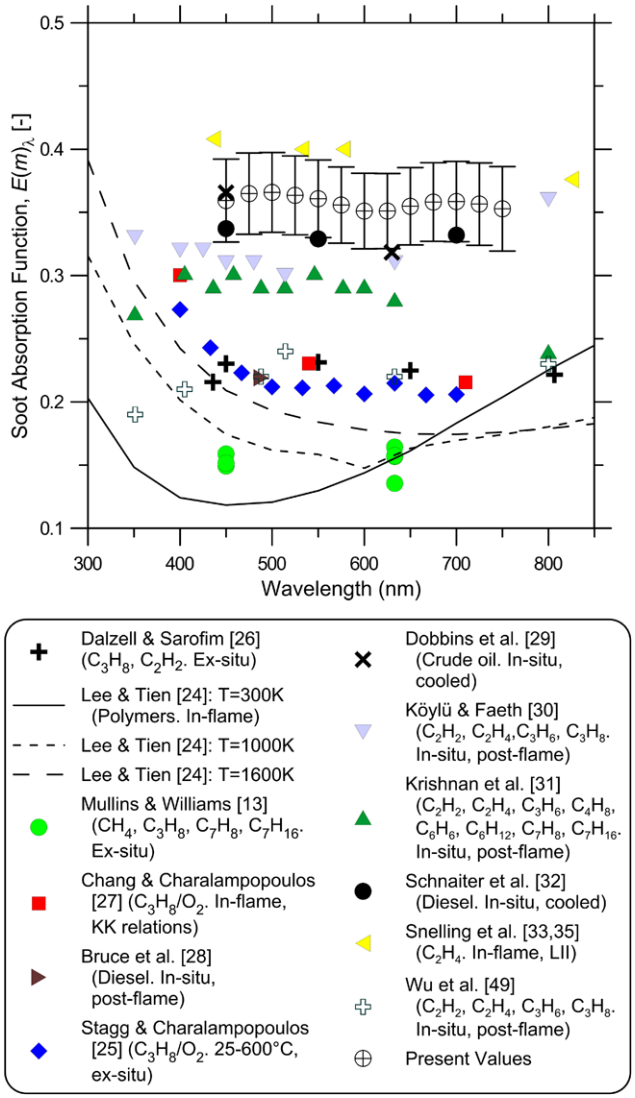

Fig. 4 Condition-averaged $E(m)_\lambda$ data plotted alongside literature values. Samples for all ex-situ measurements were collected from within a flame

ters varied have little effect on the resultant optical properties of soot. Negligible differences were found with varying dilution rate (which affects exhaust residence time and temperature history), with dilution temperature (which also affects residence time and temperature history), or with dilution gas (which would reflect post-flame oxidation effects). If the measurements made for the 12 burner conditions studied here are instead considered repeated measurements of the same values, the spread in their results can be seen as a measure of the precision uncertainty. The results of such a treatment can be seen in Fig. 4.

The relatively narrow uncertainty bars seen in the figure suggest that it is reasonable to treat the 12 conditions as repeated measurements. Under this assumption, a wavelength-dependent soot absorption function could be defined for more generalized use at a range of conditions. The variation of the absorption function with wavelength is important for optical diagnostics that rely on data from more than a single wavelength, such as two-color pyrometry and time-resolved laser-induced incandescence. As further discussed below, the present data support the view that there is little variation in $E(m)_\lambda$ within the visible wavelengths (up to 700–750 nm). This lack of variation was common to all test conditions and indicative of a universal trend.

3.1 Other expressions of optical properties

Several authors [31, 45, 60] have reported a dimensionless extinction constant as the result of their extinction measurements. This dimensionless constant, denoted K_e here, is related to the measured extinction coefficient by the following relation:

$$K_{e,\lambda} = \frac{K_{\text{ext},\lambda}\lambda}{f_v}. \tag{13}$$

Equation (13) has a similar form to (4), used to calculate $E(m)_\lambda$, only without the dependence on $\rho_{\text{sa},\lambda}$ for the scattering correction. Since some uncertainty is introduced by the scattering correction, it is useful to re-cast the present results in terms of the dimensionless extinction constant, as shown in Table 3. As with the $E(m)$ results, K_e data were plotted against many variables in an attempt to find trends. However, once again, the only correlation found was with wavelength.

Another representation of the absorption properties of particulate matter is the so-called mass absorption cross section (MAC), which is used, for example, in the atmospheric

Table 3 Summary of condition-averaged results. Uncertainties U are given as 95% confidence limits

λ [nm]	ρ_{sa}	$U_{\rho sa}$	$E(m)$	$U_{E(m)}$	K_e	U_{Ke}	MAC [$\frac{m^2}{g}$]	U_{MAC} [$\frac{m^2}{g}$]
450	0.29	0.06	0.36	0.03	8.7	0.6	8.0	0.7
500	0.27	0.06	0.37	0.03	8.8	0.6	7.3	0.6
550	0.25	0.06	0.36	0.03	8.5	0.6	6.5	0.5
600	0.23	0.05	0.35	0.03	8.1	0.6	5.8	0.5
650	0.21	0.05	0.35	0.03	8.1	0.6	5.4	0.4
700	0.20	0.05	0.36	0.03	8.1	0.6	5.1	0.4
750	0.18	0.05	0.35	0.03	7.8	0.7	4.7	0.4

particulate field [9]. MAC represents the mass-normalized absorption cross section of particulate aerosol, and is independent of the particle density since $f_v \propto 1/\rho_s$ from (5), causing the density terms to cancel in (14). MAC is related to the present experimental quantities by the following:

$$\mathrm{MAC} = \frac{K_{\mathrm{ext},\lambda}}{\rho_s(1+\rho_{\mathrm{sa}})f_v}. \tag{14}$$

The MAC values presented in Table 3 are compared with the literature below.

3.2 Comparison to literature

In Fig. 4, the condition-averaged $E(m)_\lambda$ results are plotted alongside several previous studies found in the literature. Notwithstanding the wide spread of reported results, the present results show consistency with a subset of previous studies, despite the use of significantly different fuels. In particular, the $E(m)_\lambda$ results of Dobbins et al. [29] and Schnaiter et al. [32] show similar magnitudes, and results of Krishnan et al. [31] and Snelling et al. [33] compare favorably in terms of spectral variation. The results of Köylü and Faeth [30] at the lower wavelengths were also in reasonable agreement, although they showed a significant increase of $E(m)_\lambda$ between 632 and 800 nm which was not observed in the present study. The agreement between present and past results further bolsters the generally accepted notion that soot optical properties are reasonably independent of fuel type, since the present study and the five listed above use fuels ranging from research-grade methane to diesel and crude oil.

One common assumption made is that $E(m)$ is constant across the visible wavelengths. The present results show that this approximation is reasonable, although a small but consistent dip at around 600 nm was common to all measurements. However, the magnitude of this dip is small compared to the measurement uncertainty. The present results for $E(m)_\lambda$ are not consistent with several of the other earlier studies. The absolute magnitude of $E(m)_\lambda$ is greater than that observed by groups such as Chang and Charalampopoulos [27], Lee and Tien [24], and Stagg and Charalampopoulos [25], and equally importantly we do not see the rise in $E(m)_\lambda$ below 500 nm seen by these authors. What these three groups share is that their models are based on the assumption that graphitic properties can be applied to soot. This assumption results in a rise in $E(m)_\lambda$ below 500 nm as the graphite UV resonance is approached [9, 61]. We observe no such near-UV approach to resonance in soot, similar to the findings of Krishnan et al. [31] and of Köylü and Faeth [30]. This calls into question the attribution of graphitic optical properties to soot. Additionally, early in-situ work such as that of Chang and Charalampopoulos [27] should be regarded with some caution not only because of the graphitic dispersion assumption, but also because they did not characterize their soot aggregate properties and assumed spherical soot particles and Mie theory to interpret their scattering results, which has been proven ineffective in more recent studies [62, 63].

The comparison of soot absorption function can be extended to 1064 nm. Therssen et al. [34] have measured the ratio of $E(m)$ at 532 to that at 1064 nm by matching LII intensities for known fluences. They conclude that the $E(m)$ ratio is close to 1 in the methane flame and is higher (close to 1.1) in the premixed acetylene/air flames. This conclusion is in accord with the results of Snelling et al., who found $E(m)$ at 1064 nm to be 0.4 [33], identical to that at 532 nm [65]. This would imply that $E(m)$ is essentially constant from 450 to 1064 nm.

Many studies have reported values for the MAC, which were reviewed and presented by Bond and Bergstrom [9]. After reviewing dozens of previous studies, they concluded that the value of MAC = 10 m^2/g, commonly used in the field of atmospheric modeling [64], was erroneous. Instead, they suggested an alternative value of MAC = 7.5 ± 0.6 m^2/g at a wavelength of 550 nm, which they found as the average value of results in the literature for freshly generated combustion aerosol.[2] They considered 17 studies, and adjusted the values as required to account both for the filtration medium and for the wavelength of light used in the measurements. For the latter, it was assumed that the refractive

[2]The uncertainty has been converted to 95% confidence limits for comparison. The original uncertainty figure given in the paper was 1.2 m^2/g, corresponding to a single standard deviation.

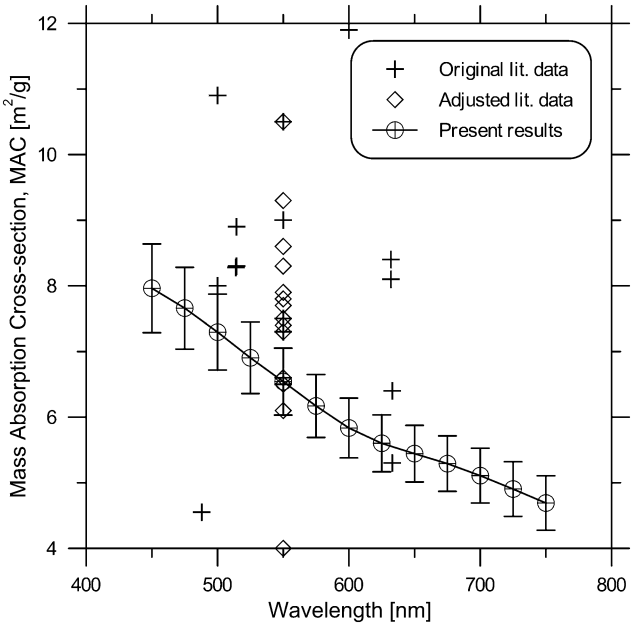

Fig. 5 Comparison of present MAC results to the literature values reviewed and adjusted by Bond and Bergstrom [9]

index of soot is constant across the visible range, resulting in an inverse relationship between MAC and wavelength. The present results support this assumption, and the uncertainty limits of their recommended value overlaps those of the present findings (6.5 ± 0.5 m^2/g) at that wavelength. Figure 5 shows a comparison between the present results and the literature values (original and adjusted) reviewed by Bond and Bergstrom [9].

4 Conclusions

The objectives of this work were to measure, with quantified uncertainties, the optical properties of soot from an inverted methane flame that had been allowed to age and cool in the exhaust stream. These conditions were selected to better reflect real-world measurement locations such as exhaust from a tailpipe or smokestack, rather than the typical in-flame diagnostics performed in the laboratory. The resulting values of the soot absorption function, $E(m)_\lambda$, displayed no distinct correlation with wavelength. This spectral variation was remarkably constant in the visible range (0.35 ± 0.03 at wavelengths of 450–750 nm) for wide variations in the cooling and dilution conditions in the exhaust. Cast in the form of mass absorption cross section, we obtain a value of 6.5 ± 0.5 m^2/g at 550 nm, which compares well to the value of 7.5 ± 0.6 m^2/g proposed by Bond and Bergstrom [9] in their meta-analysis of published literature. Comparatively little variation was found in $E(m)_\lambda$ at fixed wavelength for differences in dilution rate, dilution temperature, and dilution gas. No correlations were found between any of these properties and the physical soot properties, varied burner parameters, or other derived parameters.

While the large spread in previous data seen in Fig. 4 precludes widespread agreement of results, the present values (which include quantified uncertainties) compare well with a subset of studies found in the literature. In particular, the $E(m)_\lambda$ results of Dobbins et al. [29] and Schnaiter et al. [32] show similar magnitudes, and results of Krishnan et al. [31] and Snelling et al. [33] compare favorably in terms of spectral variation. This agreement supports the notion that fuel type has little effect on optical properties of cooled, post-flame soot, as these four studies all use different, widely varied fuels; both liquid and gaseous, from crude oil to research-grade methane. Thus, these results are encouraging for the combustion diagnostics community, as they show that cooled soot from a methane flame is comparable to other measurements made for cooled or aged soot [29, 32], for soot measured shortly post-flame [31], and for in-flame soot [33].

Acknowledgements Financial support for this work was provided by the Natural Resources Canada Program of Energy Research and Development (project manager, Michael Layer) and the Natural Sciences and Engineering Research Council (NSERC) of Canada. Mr. Coderre was additionally supported by the National Research Council Graduate Student Scholarship Supplement Program (GSSSP).

Appendix: Uncertainty analysis

Experimental results are somewhat meaningless without an idea of the accuracy of the measurements. The uncertainties associated with the values obtained were estimated based on the method outlined by the ASME [65]. The total uncertainty consists of two distinct parts, the bias uncertainty and the precision uncertainty. Bias uncertainty occurs due to the inaccuracy of the measuring equipment, whereas precision uncertainty occurs due to random scatter of the data. These two types of uncertainty are evaluated individually and then combined to find an estimate of the total uncertainty. The following is a summary of the sources of uncertainty in the present analysis. Please refer to [43] for further detail.

A.1 Gravimetric soot volume fraction

The soot volume fraction determined by gravimetric analysis is dependent on the mass of the collected soot, the volume of gas that was filtered, the ambient and gas temperatures, and the mass density of soot. The remaining uncertainty in the mass of soot is captured in the repeatability of the balance, which was found to be an order of magnitude greater than the quoted accuracy of the balance and was therefore the dominant uncertainty for the mass measurement. Since the mass of soot determined is the result of

two separate mass measurements, this uncertainty was multiplied by $\sqrt{2}$. The uncertainty associated with the volume measurement corresponded to the uncertainty in the sample duration combined in quadrature with the quoted uncertainty of the MFC (mass flow controller). Uncertainties in the ambient and exhaust gas temperatures were inflated to account for additional sources of uncertainty such as soot build up over the course of a given sampling. The uncertainty in the mass density of soot corresponds to the spread of the values reported in the literature at a 95% confidence interval. The bias limit was found by combining the contributions of each term in (5) in quadrature:

$$\frac{U_{f_v}}{f_v} = \sqrt{\left(\frac{U_{m_s}}{m_s}\right)^2 + \left(\frac{U_V}{V}\right)^2 + \left(\frac{U_{T_\infty}}{T_\infty}\right)^2 + \left(\frac{U_{T_s}}{T_s}\right)^2 + \left(\frac{U_{\rho_s}}{\rho_s}\right)^2}, \tag{15}$$

where U_x is the uncertainty in x. The precision uncertainty, represented by $100(1-\alpha)\%$ confidence limits associated with a mean value, $\bar{x}$, is determined by the following formula:

$$\bar{x} \pm t_{\frac{\alpha}{2},n-1}\frac{\sigma}{\sqrt{n}}, \tag{16}$$

where σ is the standard deviation, n is the number of samples, and t is the t-distribution value for a tail area of $\alpha/2$ and $n-1$ degrees of freedom.

As an example, the average bias uncertainty for all samples of a given condition was found to be 4.6%. The average soot volume fraction for the 34 samples at this condition was 54.9 parts per billion (ppb) with a standard deviation of 2.0 ppb or 3.7%. The precision uncertainty for 95% confidence was then found to be 1.3%. Combining the bias and precision uncertainties in quadrature gave a total uncertainty in the gravimetric soot volume fraction for this condition of 4.8%, or 2.6 ppb.

A.2 Extinction coefficient

The uncertainty associated with the extinction measurement is discussed by Thomson et al. [55], only in the present case the flame emission term was removed. The bias uncertainty was estimated by examining the symmetry about a vertical axis (perpendicular to the optical axis) in the normalized transmissivity data. The exhaust plume attenuates the lamp light in the central portion of the image; the edge regions of the image are unattenuated and therefore have unity transmissivity. Data were normalized using the unattenuated portion on the left-hand side of the images. Therefore, any deviations from unity transmissivity appearing in the unattenuated portion on the right-hand side were representative of a systematic (bias) uncertainty in the measurement of $\ln(\tau_\lambda)$. However, it was found that the contribution of the bias uncertainty to the total uncertainty was negligible, i.e. the total uncertainty was dominated by the precision uncertainty or repeatability.

A.3 Primary particle diameter

The uncertainty calculation for the TEM results comprised bias and precision uncertainties. Bias uncertainty was estimated based on the spatial resolution of the images. At a magnification of 18000×, the spatial calibration was 0.777778 nm/pixel, and the accuracy of the location of particle edges was estimated at ±2 pixels. That uncertainty occurs twice, finding both edges of the particle, so the resulting bias uncertainty was $2\sqrt{2} \times 0.777778 \approx 2.2$ nm. For precision uncertainty, a 95% confidence interval of ≈ 1.1 nm was typical. Combining these contributions in quadrature resulted in a total uncertainty of $\sqrt{(2.2^2 + 1.1^2)} = 2.5$ nm.

A.4 Fractal parameters

The uncertainty associated with the fractal parameters was difficult to estimate due to the empirical nature of the analysis. Uncertainties in measurement from the SEM images were obscured in the image analysis, since the images were distorted somewhat during processing and the 'true' measurement was unknown. In addition, the use of empirical constants given by Brasil et al. [20] in the projected area analysis likely introduced further uncertainty. These uncertainties were further obscured when it was the slope and intercept of a line of best fit to the data that were of significance. Nevertheless, since the slope and intercept were determined from a line of best fit using least-squares regression, the uncertainties in the fractal parameters were assumed to be equivalent to the confidence intervals in the fits. Thus, these estimated uncertainties represent the spread in the data and are therefore estimates of precision uncertainty, which was assumed to be the dominant source of uncertainty for the sake of this analysis. Again the reader is reminded that the scatter correction term in the governing extinction equation appears as $(1 + \rho_{\mathrm{sa},\lambda})$. For a $\rho_{\mathrm{sa},\lambda}$ value on the order of 0.3, a 10% increase in uncertainty in $\rho_{\mathrm{sa},\lambda}$ results in a contribution of only 3% to the total uncertainty of $E(m)_\lambda$. Also, any additional uncertainty introduced by this assumption should be small in comparison to the overall uncertainty in $\rho_{\mathrm{sa},\lambda}$.

A.5 Aggregate size distribution

The uncertainty in the distribution parameters is subject to the same difficulties as discussed above for the fractal parameters. In this case, the confidence limits in the fit parameters were much wider, giving further weight to the notion

that this representation of the precision uncertainty dominates the bias uncertainty contribution to the total. Again, in this case, the confidence limits given for the fit of the aggregate size histogram to the statistical distributions were used at face value, since they were assumed to be the dominant source of uncertainty in the distribution parameters.

A.6 Scattering-to-absorption ratio

The scattering-to-absorption ratio is dependent on many factors, and the form of the dependence is too complex to apply the bias limit determination based on combining terms in quadrature. Instead, a parametric analysis was performed, where each parameter was varied to its bias limits and the effect on the scattering-to-absorption ratio was observed. In addition, a blanket value of 10% uncertainty was added in order to capture uncertainties inherent in the use of the RDG-PFA approximation, as discussed in Sect. 2.3. The experimental parameters that contribute to $\rho_{\mathrm{sa},\lambda}$ are the fractal parameters D_f and k_g, the primary particle size d_p, and the fits of size data to statistical distributions (M_1 and τ). The total uncertainty was determined by combining the contributions of each parameter in quadrature.

A.7 Soot absorption function

The determination of the uncertainty of $E(m)_\lambda$ required only uncertainty propagation without the addition of further sources of uncertainty. With the uncertainties in all the required variables known, the total uncertainty in the absorption function $E(m)_\lambda$ can also be determined by combining individual contributions in quadrature as shown in (17).

$$\frac{U_{E(m)_\lambda}}{E(m)_\lambda} = \sqrt{\left(\frac{U_{K_{\mathrm{ext},\lambda}}}{K_{\mathrm{ext},\lambda}}\right)^2 + \left(\frac{U_{\rho_{\mathrm{sa},\lambda}}}{1+\rho_{\mathrm{sa},\lambda}}\right)^2 + \left(\frac{U_{f_\mathrm{v}}}{f_\mathrm{v}}\right)^2}. \quad (17)$$

References

1. C.A. Pope III, R. Burnett, M. Thun, E. Calle, K. Ito, G. Thurston, J. Am. Med. Inform. Assoc. **287**, 1132 (2002)
2. P. Chylek, J. Wong, Geophys. Res. Lett. **22**, 929 (1995)
3. V. Ramanathan, G. Carmichael, Nat. Geosci. **1**, 221 (2008)
4. H. Moosmüller, R. Chakrabarty, W. Arnott, J. Quant. Spectrosc. Radiat. Transf. **110**, 844 (2009)
5. C. Schulz, B.F. Kock, M. Hofmann, H. Michelsen, S. Will, B. Bougie, R. Suntz, G.J. Smallwood, Appl. Phys. B **83**, 333 (2006)
6. S. di Stasio, P. Massoli, Meas. Sci. Technol. **5**, 1453 (1994)
7. F. Liu, D.R. Snelling, K.A. Thomson, G.J. Smallwood, Appl. Phys. B **96**, 623 (2009)
8. B.M. Crosland, M.R. Johnson, K.A. Thomson, Appl. Phys. B **102**, 173 (2011)
9. T. Bond, R. Bergstrom, Aerosol Sci. Technol. **40**, 27 (2006)
10. S. De Iuliis, F. Cignoli, G. Zizak, Appl. Opt. **44**, 7414 (2005)
11. T. Williams, C. Shaddix, K. Jensen, J. Suo-Anttila, Int. J. Heat Mass Transf. **50**, 1616 (2007)
12. IEA, *Key World Energy Statistics* (International Energy Agency, 2009)
13. J. Mullins, A. Williams, Fuel **66**, 277 (1987)
14. T. Charalampopoulos, Rev. Sci. Instrum. **58**, 1638 (1987)
15. B. Vaglieco, F. Beretta, A. D'Alessio, Combust. Flame **79**, 259 (1990)
16. A. Filippov, M. Zurita, D. Rosner, J. Colloid Interface Sci. **229**, 261 (2000)
17. C. Megaridis, R. Dobbins, Combust. Sci. Technol. **71**, 95 (1990)
18. Ü.Ö. Köylü, G.M. Faeth, Combust. Flame **89**, 140 (1992)
19. C. Sorensen, Aerosol Sci. Technol. **35**, 648 (2001)
20. A. Brasil, T. Farias, M. Carvalho, J. Aerosol Sci. **30**, 1379 (1999)
21. S. Friedlander, C. Wang, J. Colloid Interface Sci. **22**, 126 (1966)
22. P.G.J. van Dongen, M.H. Ernst, Phys. Rev. Lett. **54**, 1396 (1985)
23. C. Sorensen, J. Cai, N. Lu, Appl. Opt. **31**, 6547 (1992)
24. S. Lee, C. Tien, in *Proc. 18th Int. Symp. Combustion* (1981), p. 1159
25. B. Stagg, T. Charalampopoulos, Combust. Flame **94**, 381 (1993)
26. W. Dalzell, A. Sarofim, J. Heat Transf. **91**, 100 (1969)
27. H. Chang, T. Charalampopoulos, Proc. R. Soc., Math. Phys. Sci. **430**, 577 (1990)
28. C. Bruce, T. Stromberg, K. Gurton, J. Mozer, Appl. Opt. **30**, 1537 (1991)
29. R. Dobbins, G. Mulholland, N. Bryner, Atmos. Environ. **28**, 889 (1994)
30. Ü.Ö. Köylü, G. Faeth, J. Heat Transf. **118**, 415 (1996)
31. S. Krishnan, K. Lin, G. Faeth, J. Heat Transf. **122**, 517 (2000)
32. M. Schnaiter, H. Horvath, O. Möhler, K. Naumann, H. Saathoff, O. Schöck, J. Aerosol Sci. **34**, 1421 (2003)
33. D.R. Snelling, F. Liu, G.J. Smallwood, Ö.L. Gülder, Combust. Flame **136**, 180 (2004)
34. E. Therssen, Y. Bouvier, C. Schoemaecker-Moreau, X. Mercier, P. Desgroux, M. Ziskind, C. Focsa, Appl. Phys. B **89**, 417 (2007)
35. D.R. Snelling, K.A. Thomson, F. Liu, G.J. Smallwood, Appl. Phys. B **96**, 657 (2009)
36. C. Sorensen, J. Cai, N. Lu, Langmuir **8**, 2064 (1992)
37. Ü.Ö. Köylü, G. Faeth, J. Heat Transf. **116**, 152 (1994)
38. Ü.Ö. Köylü, G. Faeth, J. Heat Transf. **116**, 971 (1994)
39. T.L. Farias, Ü.Ö. Köylü, M.G. Carvalho, Appl. Opt. **35**, 6560 (1996)
40. F. Liu, D.R. Snelling, in *AIAA 40th Thermophysics Conf.* (2008), p. AIAA 2008-4362
41. R. Siegell, J. Howell, *Thermal Radiation and Heat Transfer*, 2nd edn. (McGraw-Hill, New York, 1981)
42. C. Stipe, B. Higgins, D. Lucas, C. Koshland, R. Sawyer, Rev. Sci. Instrum. **76**, 023908 (2005)
43. A.R. Coderre, M.A.Sc. Thesis, Carleton University, Ottawa, Canada, 2009
44. W.P. Arnott, H. Moosmüller, P.J. Sheridan, J.A. Ogren, R. Raspet, W.V. Slaton, J.L. Hand, S.M. Kreidenweis, J.L. Collett Jr., J. Geophys. Res. **108**, 4034 (2003)
45. M. Choi, G. Mulholland, A. Hamins, T. Kashiwagi, Combust. Flame **102**, 161 (1995)
46. E. Taylor, Filter weighing procedure for 2007 and newer heavy duty diesel engines. West Virginia University, 2006
47. C. Tsai, C.-T. Changa, B.-H. Shiha, S.G. Aggarwala, S.-N. Lib, H.M. Cheinb, T.-S. Shihc, Sci. Total Environ. **293**, 201 (2002)
48. M. Choi, A. Hamins, G. Mulholland, T. Kashiwagi, Combust. Flame **99**, 174 (1994)
49. J. Wu, S. Krishnan, G. Faeth, J. Heat Transf. **119**, 230 (1997)
50. Ü.Ö. Köylü, G. Faeth, T. Farias, M. Carvalho, Combust. Flame **100**, 621 (1995)
51. Ü.Ö. Köylü, Y. Xing, D. Rosner, Langmuir **11**, 4848 (1995)
52. S. Duhr, D. Braun, Proc. Natl. Acad. Sci. USA **103**, 19678 (2006)
53. R. Dobbins, C. Megaridis, Langmuir **3**, 254 (1987)
54. G. Mulholland, C. Bohren, K. Fuller, Langmuir **10**, 2533 (1994)

55. K.A. Thomson, M.R. Johnson, D.R. Snelling, G.J. Smallwood, Appl. Opt. **47**, 694 (2008)
56. D.R. Snelling, K.A. Thomson, G.J. Smallwood, Ö.L. Gülder, Appl. Opt. **38**, 2478 (1999)
57. I. Ayranci, R. Vaillon, N. Selcuk, F. Andre, D. Escudie, J. Quant. Spectrosc. Radiat. Transf. **104**, 266 (2007)
58. P. Greenberg, J. Ku, Appl. Opt. **36**, 5514 (1997)
59. C. Dasch, Appl. Opt. **31**, 1146 (1992)
60. R. Dobbins, C. Megaridis, Appl. Opt. **30**, 4747 (1991)
61. E. Taft, H. Philipp, Phys. Rev. **138**, A197 (1965)
62. G. Faeth, Ü.Ö. Köylü, Combust. Sci. Technol. **108**, 207 (1995)
63. Ü.Ö. Köylü, Combust. Flame **109**, 488 (1997)
64. J. Seinfeld, S. Pandis, *Atmospheric Chemistry and Physics: From Air Pollution to Climate Change* (Wiley, New York, 1998)
65. ASME, *Part 1: Measurement Uncertainty, Instruments and Apparatus* (ANSI/ASME PTC 19.1, 1985)